OKU Fen Bilimleri Enstitüsü Dergisi
6(2): 1481-1499, 2023

OKU Journal of The Institute of Science and Technology, 6(2): 1481-1499, 2023

Osmaniye Korkut Ata Üniversitesi Fen Bilimleri Enstitüsü Dergisi

Osmaniye Korkut Ata University Journal of The Institute of Science and Technology

Large Eddy Simulation of the Biased Wake Flow Downstream of Circular Cylinders with a Slit

Tural TUNAY[1*]

[1]Adana Alparslan Turkes Science and Technology University Faculty of Engineering Department of Mechanical Engineering, Adana, Türkiye

[1]https://orcid.org/0000-0001-5994-4565
*Sorumlu yazar: ttunay@atu.edu.tr

Research Article

Article History:
Received: 08.11.2022
Accepted: 24.02.2023
Published online: 05.07. 2023

Keywords:
Cylinder
LES
Passive flow control
Slit
Biased wake flow

ABSTRACT

The characteristics of flow around slit-inserted cylinders were investigated using the three-dimensional large eddy simulation (LES). In the investigations, three different slit width-to-cylinder diameter ratios, i.e., s/D = 0.1, 0.2 and 0.3, together with regular cylinder were used. Slits were placed inside the cylinders with a zero-inclination angle, $\beta = 0^o$. The Reynolds number of the flow was $Re_D = 3900$ based on the cylinder diameter, D, and free stream velocity, U_∞. The results presented that the jet flow emerging from the slits deviated in crossflow direction forming a biased wake flow downstream of the slit cylinders. Compared with the regular cylinder, relative per cent reductions in drag coefficients of the slit cylinders with s/D = 0.1, 0.2 and 0.3 were 3.1%, 11.3% and 6.5%, respectively. The rates of turbulence quantities in downstream wakes of the slit cylinders were reduced. Formations of shear layers in the downstream wake changed drastically as the slit width-to-diameter ratio, s/D, increased.

Yarıklı Dairesel Silindirlerin Yönlenmiş Aşağı Girdap Akışının Büyük Girdap Simülasyonu

Araştırma Makalesi

Makale Tarihçesi:
Geliş tarihi: 08.11.2022
Kabul tarihi: 24.02.2023
Online Yayınlanma: 05.07.2023

Anahtar Kelimeler:
Silindir
BGS (Büyük girdap simülasyonu)
Pasif akış kontrolü
Yarık
Yönlenmiş girdap akışı

ÖZ

İçerisine yarık yerleştirilmiş silindirlerin etrafındaki akışın özellikleri, üç boyutlu büyük girdap simülasyonu (BGS) kullanılarak araştırılmıştır. Araştırmalarda, normal silindir ile birlikte üç farklı yarık genişliği-silindir çapı oranına, örneğin, s/D = 0.1, 0.2 ve 0.3, sahip silindirler kullanılmıştır. Yarıklar silindirlerin içine serbest akış yönüyle sıfır eğim açısı, $\beta = 0^o$, yapacak şekilde yerleştirilmiştir. Silindir çapına, D, ve serbest akış hızına, U_∞, bağlı olarak akışın Reynolds sayısı $Re_D = 3900$'dür. Sonuçlar, yarıklardan çıkan jet akışının çapraz akış yönünde yönlendiğini ve silindirlerin girdap bölgesinde yönlenmiş bir akış yapısı oluşturduğunu ortaya koymaktadır. Normal silindir ile karşılaştırıldığında, s/D = 0.1, 0.2 ve 0.3 olan yarık silindirlerin sürükleme katsayılarındaki göreceli yüzde azalmalar sırasıyla %3.1, %11.3 ve %6.5'dir. İçerisine yarık yerleştirilmiş silindirlerin aşağı bölgesinde oluşan girdaplı akış yapısının maksimum türbülans değerinin azaldığı tespit edilmiştir. Yarık genişliği-silindir çapı oranı, s/D, değeri arttıkça, silindirlerin aşağı akış bölgesinde oluşan kayma tabakalarının oluşumları büyük ölçüde değiştiği gözlenmiştir.

To Cite: Tunay T. Large Eddy Simulation of the Biased Wake Flow Downstream of Circular Cylinders with a Slit.. Osmaniye Korkut Ata Üniversitesi Fen Bilimleri Enstitüsü Dergisi 2023; 6(2): 1481-1499.

1. Introduction

Circular cylinders have simple geometries that exhibit most of the flow characteristics occurring in the flow around bluff bodies. For example, the flow around a cylinder has a large-unsteady downstream wake with shear layers on both sides. Thus, understanding of the characteristics of flow around circular cylinders gives essential information about the general characteristics of the flow around bluff bodies that exist in many industrial applications, with relatively low computational costs. Additionally, the study of the flow around circular cylinders helps to develop new flow control methods and assess their efficiency.

There are various ways of controlling the characteristics of flow around cylinders, which can be classified into two groups, e.g., active and passive flow control methods. Among them, inserting a slit inside a cylinder is one way of the passive flow control methods around a circular cylinder. Both Igarashi (1978, 1982) and Bao et al. (2018) conducted studies to understand the effects of different inclination angles of the slits on the flow characteristics around the circular cylinder at different Reynolds numbers. Despite the difference in their Reynolds numbers, both of them defined three different flow patterns around the circular cylinder for a different range of the inclination angle of the slit. For the range of $0^o \leq \beta \leq 40^o - 45^o$, a lower mean drag coefficient and root-mean-square lift coefficient were reported due to an increase in the base pressure and downstream movement of the vortex formation region which were caused by the self-injection of the fluid flow into the wake region. Bao et al. (2018) stated that the relative reduction ratio of the mean drag coefficient reached the maximum of 28.6% at s/D = 0.3 and $\beta = 0^o$. For the range of $40^o - 45^o \leq \beta \leq 60^o$, both studies found that the effects of the slit on the flow characteristics were too small. For the range of $60^o \leq \beta \leq 90^o$, the reduction in base pressure coefficient and shedding frequency due to boundary layer suction was observed which caused a greater mean drag coefficient and root-mean-square lift coefficient than the regular cylinder. Olsen and Rajagopalan (2000) observed that the relationship between the Strouhal and the Reynolds numbers was significantly different for the cylinder with a slit normal to the flow where St_D was always higher than for a circular cylinder over the range of $60 < Re_D < 1000$. Junwei et al. (2012) presented that the vortex shedding frequency of the slit cylinder was faster than the regular cylinder.

A slit with zero-inclination angle, $\beta = 0^o$, placed inside a cylinder connects the front and rear stagnation regions on the cylinder at which there is a high-pressure difference between them. Thus, it balances the pressure difference between the front and rear surfaces of the cylinder by increasing pressure in the downstream wake of the cylinder. Accordingly, in the previous literature, Sheng and Chen (2016) reported a favourable reduction of drag and lift coefficients with rising the width of the slit with $\beta=0^o$. Baek and Karniadakis (2009) stated that a slit in circular cylinders would be effective in suppressing vortex-induced vibrations by either weakening or detuning the vortex shedding. Ordia et al. (2017) found that the slit width was an important parameter in determining the strength of the vortices. At higher slit widths, the configuration behaved like a dual bluff body, and strong crisscross

vortex shedding was observed. Gao et al. (2917a,b) presented bi-stable flow patterns in the near wake of the slit cylinder with $\beta = 0^o$ with s/D = 0.075. They concluded that bi-stable flow occurs due to interaction between the symmetric-mode jet vortices and the asymmetric-mode shear layer instability behind the cylinder. Ordia et al. (2017) defined different flow regimes according to the Reynolds number for the flow around the slit cylinder with $\beta = 0^o$. Whereas at low Reynolds numbers, i.e., $Re_D < 500$, the vortex shedding occurred only in the outer shear layers, at higher Reynolds numbers, i.e., $Re_D > 1000$, the vortex shedding occurred in both the inner and the outer shear layers. The wake flow downstream of the slit cylinder at a higher Reynolds number exhibits more complex interactions between the shear layers and vortices that need to be understood in detail. The wake flow downstream of the regular circular cylinder at higher Reynolds numbers, i.e., between $1000 < Re < 2 \times 10^5$, was defined as a shear-layer transition regime by Williamson (1996). In this range of the Reynolds numbers, the wake flow was characterized by increased base suction and 2-D Reynolds stress levels together with decreased Strouhal number and the formation length of the mean recirculation region compared with lower Reynolds numbers flow. The previous numerical studies on the investigation of the flow characteristics around the slit cylinders have been mainly conducted at the Reynolds numbers below $Re_D = 500$ by using 2-D computational flow fields. Thus, there is a need to understand the unsteady and three-dimensional characteristics of the flow field around the slit cylinders at higher Reynolds numbers by using accurate turbulence-resolving simulations, e.g., large eddy simulation (LES).

The present study investigated the characteristics of the flow field around the slit-inserted cylinders with three different slit width to cylinder diameter ratios, i.e., s/D = 0.1, 0.2, and 0.3. Three-dimensional large eddy simulations (LES) was used to resolve the flow field. The Reynolds number of the flow was $Re_D = 3900$ based on the diameter of the cylinder, D, and the free-stream velocity, U_∞.

2. Test Cases and Numerical Method

2.1. Test Cases and Geometry of the Computational Domain

The geometric details of the test cases used in the present study were shown in Figure 1(a). As presented in the figure, three different slit width-to-cylinder diameter ratios, s/D, were used in the investigations. The diameters of all cylinders were the same and equal to D = 0.05 m. Slits were placed inside the cylinders with a zero-inclination angle to the free-stream flow, $\beta = 0^o$, so that they were parallel to the direction of the incoming free-stream flow. The height of the cylinders was equal to the height of the computational domain. Additionally, Figure 1(b) shows the geometric details of the computational flow domain. The length, width, and height of the computational flow domain in terms of the cylinder's diameter were $40D \times 20D \times \pi D$, respectively. The cylinders were located in the channel such that the upstream length between its centre and inlet of the channel was 10D in the

direction of the flow, i.e., x-direction. The cylinders were also located at mid-point in the crossflow direction, i.e., z-direction.

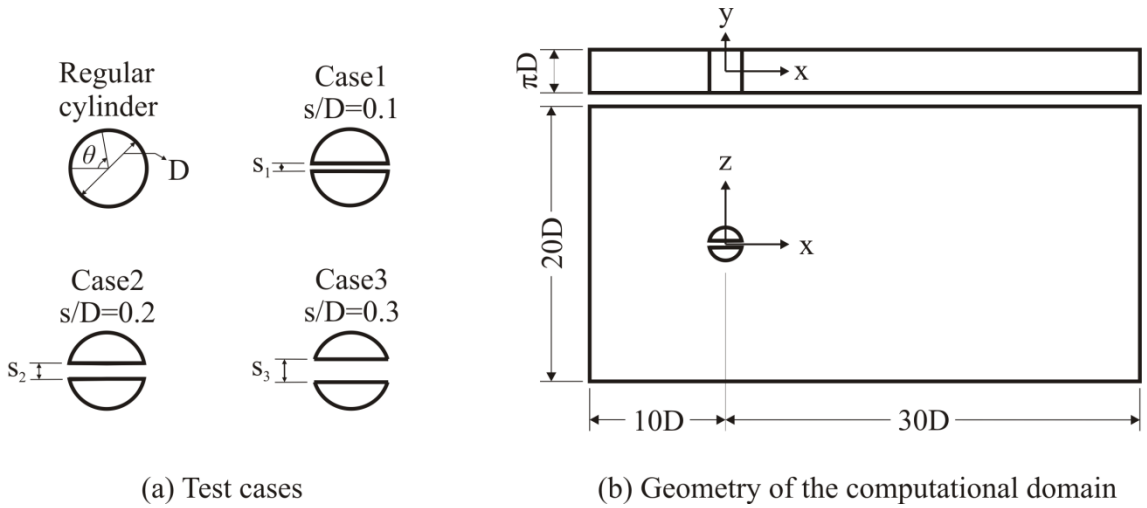

Figure 1. Test cases and geometric dimensions of the computational domain.

2.2. Governing Equations and Numerical Methods

Space-filtered incompressible continuity and Navier-Stokes equations given in Equations (1) and (2) were used in the solutions of the turbulent flow field around cylinders with the aid of the large eddy simulation (LES).

$$\frac{\partial \bar{u}_i}{\partial x_i} = 0 \tag{1}$$

$$\frac{\partial \bar{u}_i}{\partial t} + \frac{\partial}{\partial x_j}\left(\bar{u}_i \bar{u}_j\right) = -\frac{1}{\rho}\frac{\partial \bar{p}}{\partial x_i} + \nu \frac{\partial^2 \bar{u}_i}{\partial x_j \partial x_j} - \frac{\partial \tau_{ij}}{\partial x_j} \tag{2}$$

Governing equations given in Equations (1) and (2) were discretized using the finite volume method. Pressure-based segregated algorithm including SIMPLEC and PRESTO methods were used. The point implicit (Gauss-Seidel) linear equation solver in conjunction with an Algebraic Multigrid (AMG) method were used to solve the resultant scalar system of equations. Commercial CFD software, Ansys Fluent, was used for the calculations. The time step used in the computations was 0.0025s. The total simulation time in all simulations was 160s. The last 120 seconds of the simulations were used to compute time-averaged values of the flow variables.

2.3. Boundary Conditions and Computational Mesh

Boundary conditions used in the computations are presented in Figure 2. A steady uniform velocity profile, U_∞ = 0.078297 m/s with a zero-turbulence rate, was used as an inlet boundary condition. At the outlet, diffusion fluxes for all flow properties in the exit direction were assumed to be zero. The surfaces of the cylinders were treated as a no-slip boundary condition. The top and bottom surfaces of the channel were set as periodic boundary condition which uses the flow conditions at the fluid cell

adjacent to the opposite periodic plane. Lateral surfaces of the channel were treated as slip surfaces using symmetry boundary conditions. The initial conditions of the flow cases were computed from the previous solution of the steady RANS simulations. The Reynolds number of the flow was Re_D=3900 which is based on the free-stream velocity of the flow, U_∞ = 0.078297 m/s, and diameter of the cylinders, D = 0.05 m.

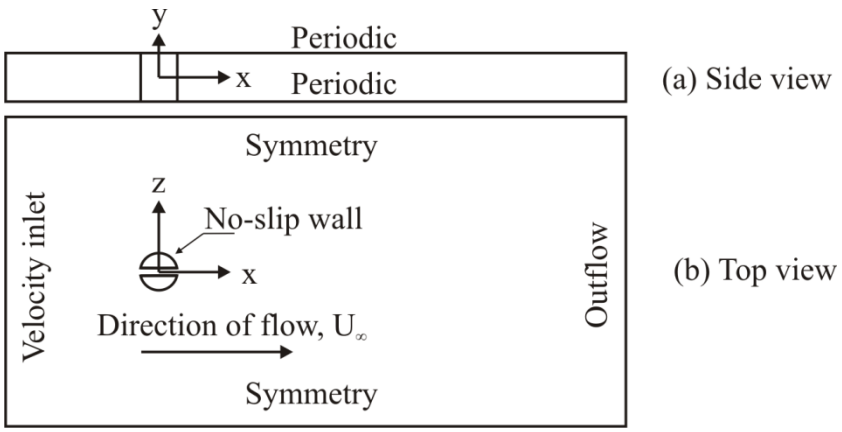

Figure 2. Boundary conditions of the computational fluid domain.

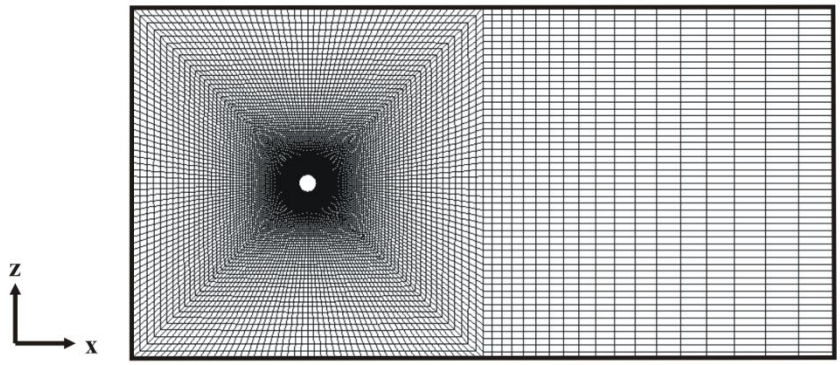

Figure 3. The general structure of the computational grid.

The general structure of the computational grid is shown in Figure 3. For the mesh independency study of the computational grid, six different meshes are used. The lowest and the highest number of computational cells employed in the meshes are 992160 and 2612792, respectively. Their details are given in Table 1. In the table, the results of the drag coefficient, C_D, the location of the separation point, θ_{SP}, the length of downstream wake, L_w/D, and the dimensionless wall distance, y^+, were compared while improving the structure of the meshes. The results of the meshes were also compared with the experimental results obtained from the literature. In the table, h_v represents the distance between the first grid point of the meshes and the cylinder surfaces. Stretching mesh was used in the vertical direction of the cylinder surface. In addition to that, uniform meshes are used on the circumference and through the height of the cylinders and they are represented by h_θ and h_y in Table 1, respectively. The results of the regular cylinder-mesh 5 showed similar results to the results of the regular cylinder-mesh 6. Besides, their drag coefficient and separation point results were close to the

corresponding results of Afgan et al. (2011) and Kravchenko and Moin (2000). Thus, the mesh structure in the regular cylinder - mesh 5 was selected for use in the investigations.

Table 1. The details of the meshes used in the independency study and the comparison of their results with the results taken from the previous literature.

Studies	C_D	θ_{SP} (^{o})	L_w/D	y^+_{max}	h_v (mm)	h_θ (mm)	h_y (mm)
Regular cylinder – mesh 1	1.142	90.0	1.582	4.01	0.5	0.98	2
Regular cylinder – mesh 2	1.056	87.8	1.940	1.98	0.25	0.98	2
Regular cylinder – mesh 3	1.055	87.8	1.822	0.79	0.1	0.98	2
Regular cylinder – mesh 4	1.025	87.0	1.954	0.80	0.1	0.875	2
Regular cylinder – mesh 5	1.004	86.6	2.104	0.80	0.1	0.75	2
Regular cylinder – mesh 6	1.004	86.6	2.105	0.80	0.1	0.75	1.625
Afgan et al. (2011)	1.020	86					
Kravchenko and Moin (2000)	1.040	88					

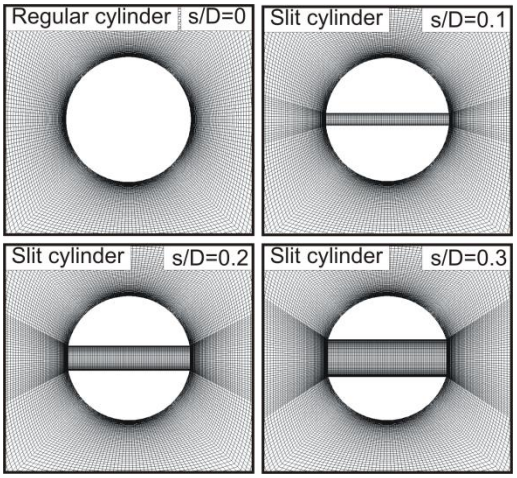

Figure 4. Close view of the computational grid around the cylinders used in the study.

In constructing the meshes for slit cylinders, while keeping the same mesh structure of the regular cylinder, new meshes which are compliant with the mesh structure around the regular cylinder were added in the slits. A close view of the mesh structures around the regular and slit cylinders are given in Figure 4.

The near wall region around the cylinders contained most of the computational cells to resolve the boundary layers on the cylinder surfaces properly. As presented in Figure 5, the maximum values of the dimensionless wall distance, $y^+_{max} < 0.8$, on both regular and slit cylinders.

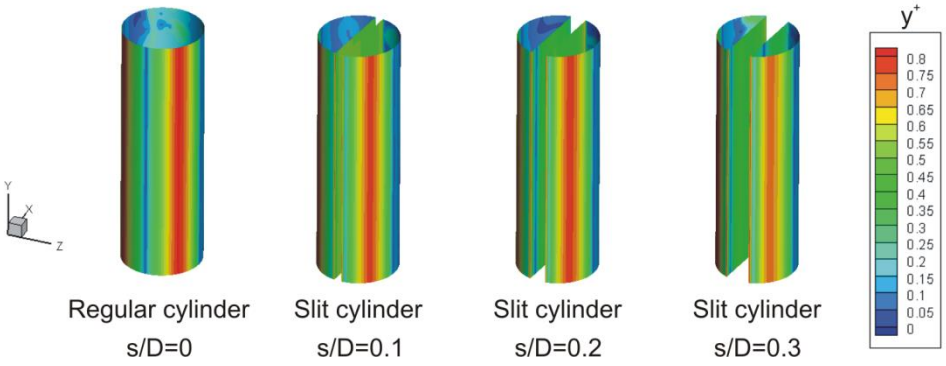

Figure 5. The value of dimensionless wall distance, y^+, on the cylinder's surfaces.

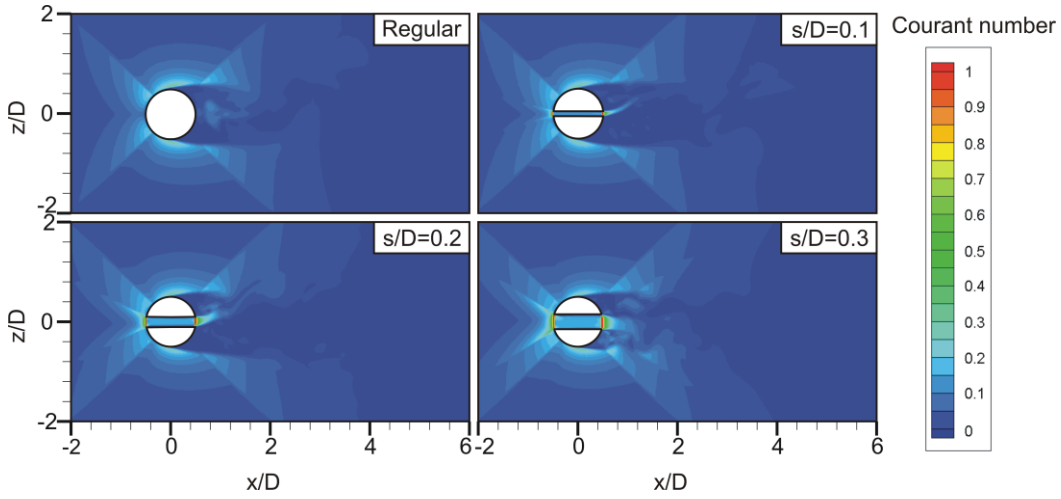

Figure 6. The contours of instantaneous cell courant number.

Figure 6 shows the values of the instantaneous cell courant number around the cylinders. In general, the values of the cell courant number were well below 1. The maximum values of the cell courant number in the cases of regular cylinder and slit cylinders with s/D = 0.1, 0.2 and 0.3 were 0.32, 0.90, 0.93, 0.98, respectively.

3. Results and Discussion

In this section, the results of the large eddy simulations (LES) of the flow around the regular and the slit cylinders were presented and discussed in detail. The study aimed to investigate the characteristics of flow around the slit cylinders. The silts were inserted inside the cylinders with zero inclination angle, $\beta = 0^o$ to the free-stream flow. Three different slit width to cylinder diameter ratios were used, e.g., s/D = 0.1, 0.2 and 0.3. The Reynolds number of the flow was $Re_D = 3900$ based on the cylinder's diameter, D, and incoming free stream flow, U_∞.

3.1. Pressure Field Results

The time-averaged pressure coefficient, $\langle C_p \rangle$, results around the regular and the slit cylinders were given in Figure 7. The results of the regular cylinder presented well-known characteristics of the flow around the circular cylinders in which there was an axial symmetry between the flow structures in the

crossflow direction. There were a high-pressure stagnation region in the upstream part and a low-pressure wake region in the downstream part of the regular cylinder. On the other hand, after placing the slit inside the cylinders, the symmetry of the flow field around the regular cylinder deteriorated gradually with increasing the slit width to cylinder diameter ratio, s/D. The minimum values of the pressure in downstream wakes of the slit cylinders with s/D = 0.1 and 0.2 increased which caused the reductions in their drag coefficients. Asymmetric locations of the minimum pressure regions occurred in the downstream wake of the slit cylinders whereas only one symmetric minimum pressure region occurred in the downstream wake of the regular cylinder. These asymmetries in $\langle C_p \rangle$ contours generated biased wake flows in the downstream wake of the slit cylinders. The location of the minimum pressure region in the downstream wake came closer to the rear end of the cylinders with s/D = 0.2 and 0.3.

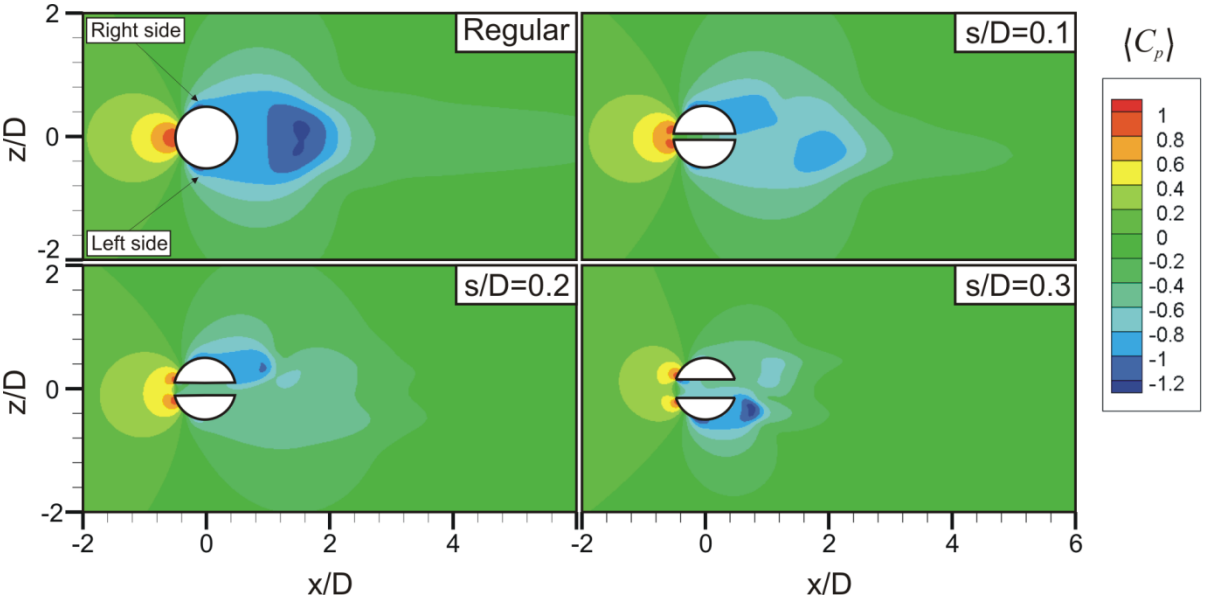

Figure 7. Contours of mean pressure coefficient, $\langle C_p \rangle$, in the vertical symmetry plane at y/D=0.

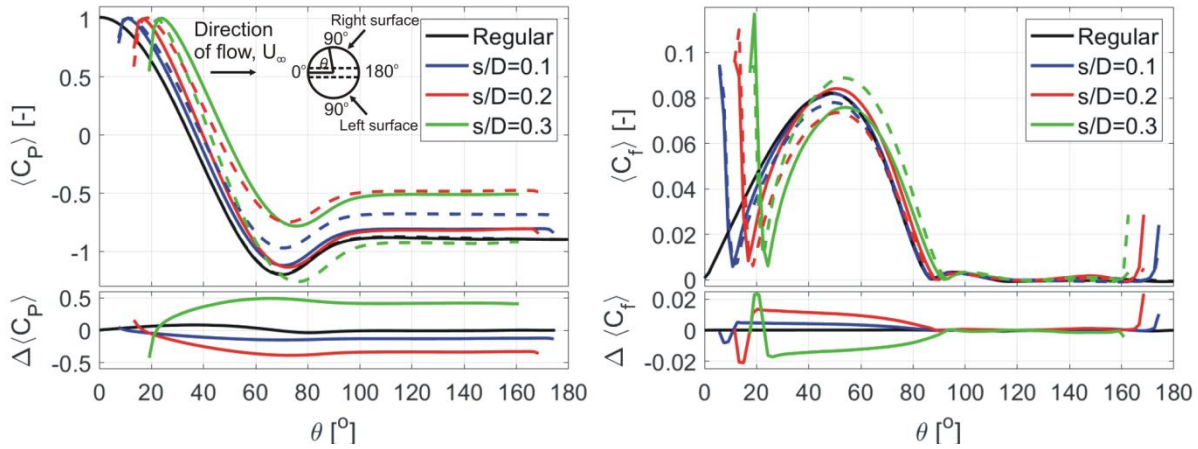

Figure 8. Results of time-averaged pressure coefficient, $\langle C_p \rangle$, and skin-friction coefficient, $\langle C_f \rangle$, on the circumference of the regular and the slit cylinders at y/D = 0. Solid and dashed lines show the results on the right and left surfaces of the cylinders, respectively.

The biases observed in the formation of the $\langle C_p \rangle$ contours in the wake flow downstream of the slit cylinders could be related to the interaction of the upstream flow with the slit geometry of the cylinders. In Figure 8, a comparison between the results of the time-averaged pressure coefficient, $\langle C_p \rangle$, and skin-friction coefficient, $\langle C_f \rangle$, on the right and left surfaces of the cylinders were given. The designations of the right and the left surfaces of the cylinders were shown in Figure 8.

In the subfigures of Figure 8, the differences between the $\langle C_p \rangle$ and the $\langle C_f \rangle$ results on the right and the left surfaces were also given at each location on the cylinder's surfaces. Results of the regular cylinders showed small differences which were the reason for the symmetry of the flow field around it. However, in the case of the slit cylinders, differences between the results on the right and the left surfaces increased as their s/D values increased. Differences started at the beginning of the surfaces on the upstream part of the cylinders, i.e., at θ_0 = 0°, 5.7°, 11.5°, 17.5° for the regular and the slit cylinders with s/D = 0.1, 0.2 and 0.3, respectively. Then, the differences changed their signs around the stagnation points, θ_S, on the upstream part of the cylinders. Locations of the stagnation points, θ_S, and the separation points, θ_{SP}, on the right and the left surfaces of the cylinders were given in Table 2. The differences in the $\langle C_p \rangle$ results reached their absolute maximums before the separation points, and then they became fixed in the separated flow region on the downstream part of the cylinders. On the other hand, the $\langle C_f \rangle$ results showed significant differences between the right and the left surface before the separation points on the upstream part of the cylinders. As a result, the bias in the locations of the minimum $\langle C_p \rangle$ in the downstream wake of the cylinders were on the same side as the cylinders' surfaces on which the values of $\langle C_f \rangle$ was higher on their upstream part and $\langle C_p \rangle$ was lower on their downstream part.

Table 2. Locations of the stagnation points, θ_S, and the separation points, θ_{SP}, on the right and the left surfaces of the cylinders.

		Regular	s/D = 0.1	s/D = 0.2	s/D = 0.3
Stagnation Point, θ_S(°)	Right surface	0	10.8	16.7	24
	Left surface		11.3	18.2	22.4
Separation Point, θ_{SP}(°)	Right surface	86.6	88.3	90	91.7
	Left surface	86.6	88.3	88.3	93.4
$\theta_{SP} - \theta_S$(°)	Right surface	86.6	**77.5**	**73.3**	67.7
	Left surface	86.6	77	70.1	**71.0**

Comparisons of the locations of the stagnation and the separation points between the right and the left surfaces of the cylinders were given in Table 2. In line with the results of $\langle C_p \rangle$ and $\langle C_f \rangle$ presented in Figure 8, there were asymmetry between the locations of the stagnation and the separation points on the right and left surfaces of the slit cylinders with s/D = 0.2 and 0.3. For example, the flow separations occurred with a delay of $\Delta\theta$ = 1.7° on the right and the left surfaces of the slit cylinders with s/D = 0.2 and 0.3, respectively. Comparisons given in Table 2 revealed that the bias of the wake

flow was on the same side of the cylinder on which there was a larger distance between the stagnation and the separation points, i.e., $\theta_{SP} - \theta_{S,Front}$ = 77.5°, 73.3° and 71.0°, on the right and left surfaces of the slit cylinders with s/D = 0.1, 0.2 and 0.3, respectively. That meant the locations of flow separations delayed on the surfaces of the slit cylinders which were on the same side as the crossflow direction of the biased flow in the downstream wake.

Table 3. Time-averaged drag $\langle C_D \rangle$ and lift $\langle C_L \rangle$ coefficients.

Force coefficients	Regular	s/D = 0.1	s/D = 0.2	s/D = 0.3
$\langle C_D \rangle$	1.004	0.973	0.891	0.939
$\langle C_L \rangle$	0.0025	0.140	0.380	-0.522

Time-averaged drag, $\langle C_D \rangle$, and lift, $\langle C_L \rangle$, coefficients of the cylinders were given in Table 3. Compared with the regular cylinder, $\langle C_D \rangle$ values of the slit cylinders decreased in amounts between 3% and 11.3%. The smallest $\langle C_D \rangle$ was obtained from the slit cylinder with s/D = 0.2. However, its $\langle C_L \rangle$ increased significantly due to the biased wake flow. In line with the crossflow direction of the biased flow in the downstream wake of the slit cylinders, $\langle C_L \rangle$ of the slit cylinders took either positive or negative values.

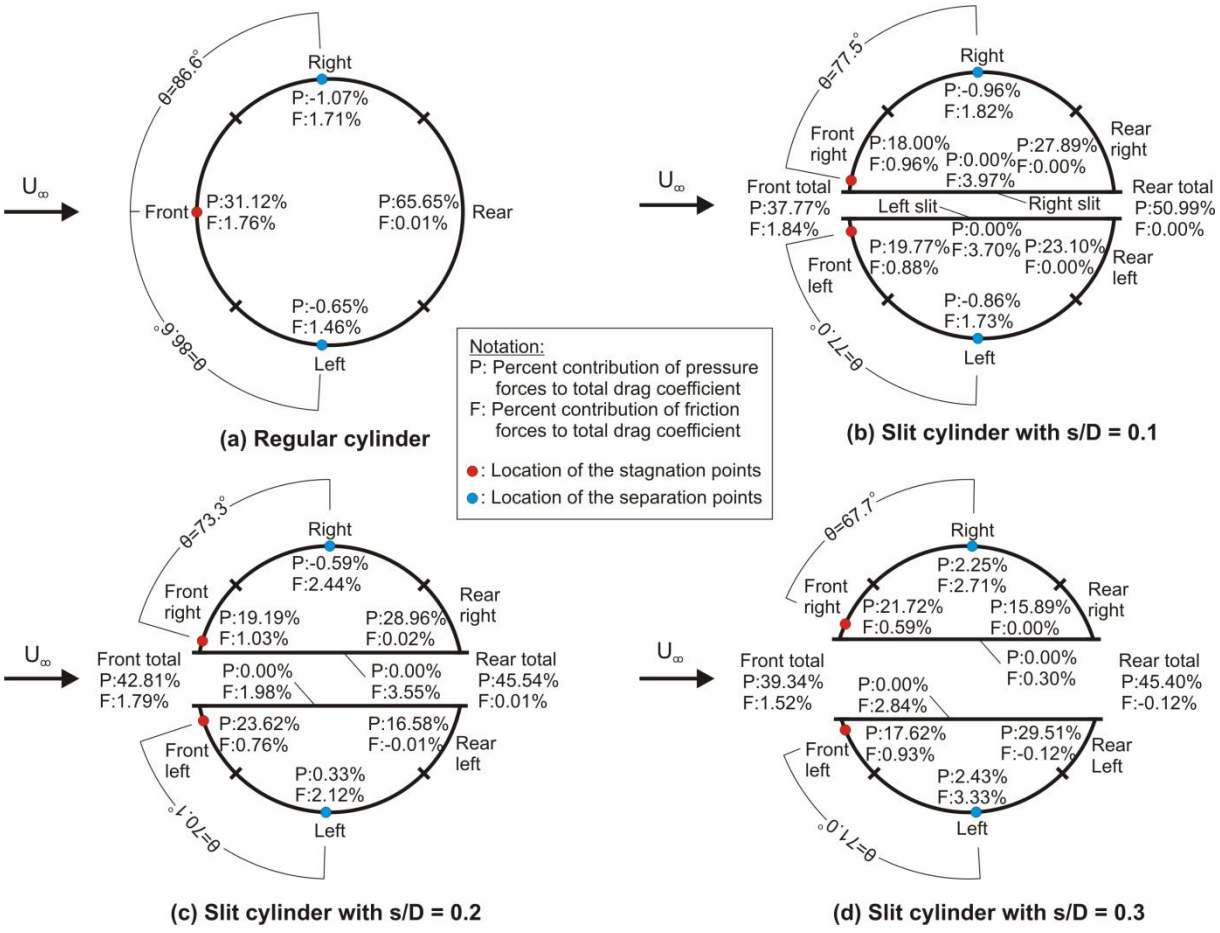

Figure 9. Per cent contribution of the cylinders' surfaces to their drag coefficients, $\langle C_D \rangle$.

In order to understand the relations between the $\langle C_D \rangle$ and s/D, decomposition of the $\langle C_D \rangle$ based on contributions of the cylinders' surfaces were investigated in both Figures 9 and 10. In all slit cylinders, as presented in Figure 9, there were asymmetry between the contributions of the right and left parts on the front and the rear surfaces of the cylinders to the $\langle C_D \rangle$ which deteriorated the balancing forces on the cylinders. Results given in the figures showed that the rear surface of the regular cylinder contributed to its $\langle C_D \rangle$ the most with an amount of 65.66%. The slits decreased the contribution of the rear surface to $\langle C_D \rangle$ considerably until s/D = 0.2, e.g., a maximum 20.11% reduction was achieved with a slit cylinder with s/D = 0.2. However, a further increase of the slit width to s/D = 0.3 lost the benefits and caused an increase in the contribution of both the rear and the side surfaces to $\langle C_D \rangle$ as shown in Figure 10. The increase in the contribution of the side surfaces to $\langle C_D \rangle$ could be related to the shifting of the stagnation points on the front surfaces of the cylinders towards the sides which caused an increase in pressure forces on the side surfaces.

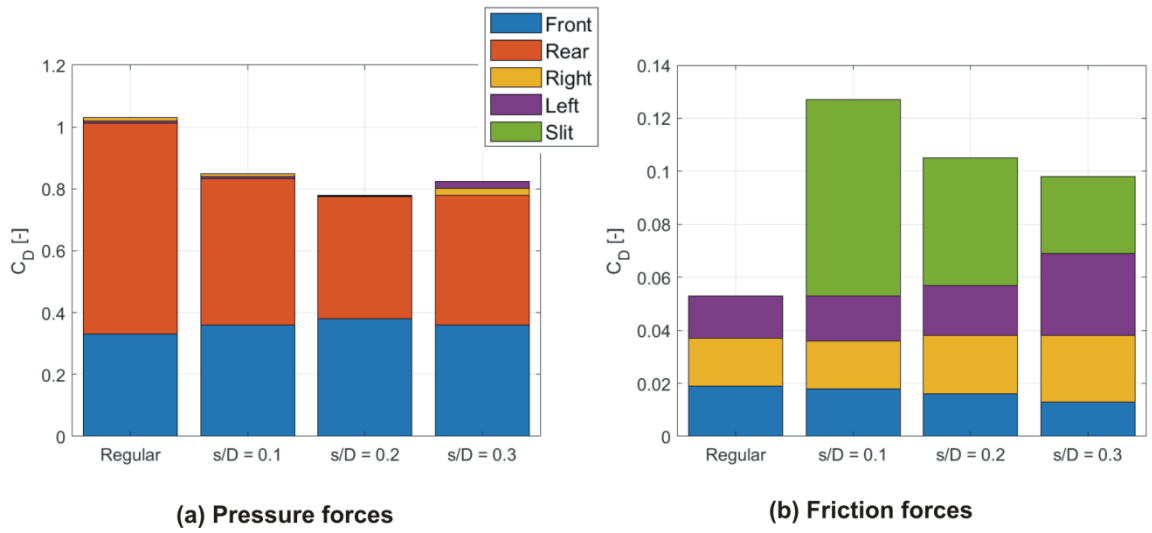

Figure 10. Decomposition of the time-averaged drag force coefficients, $\langle C_D \rangle$, based on the contributions of the pressure and the friction forces on the surfaces of the cylinders.

The spectral analysis of the lift coefficient of the cylinders are given in Figure 11. As the results of spectral analysis, the main frequencies obtained in the cases of the regular cylinder and cylinders with s/D = 0.1, 0.2 and 0.3 were f = 0.32, 0.37, 1.09 and 1.22, respectively. In addition to the main frequencies, there were secondary frequencies in the cases of slit cylinders with s/D = 0.1, 0.2 and 0.3, which were f = 1.07, 2.22 and 2.42, respectively. The main frequencies of the regular and slit cylinders with s/D = 0.1, 0.2 and 0.3 corresponded to the Strouhal numbers of $St = \frac{fD}{U_\infty} = 0.2$, 0.24, 0.70 and 0.78, respectively.

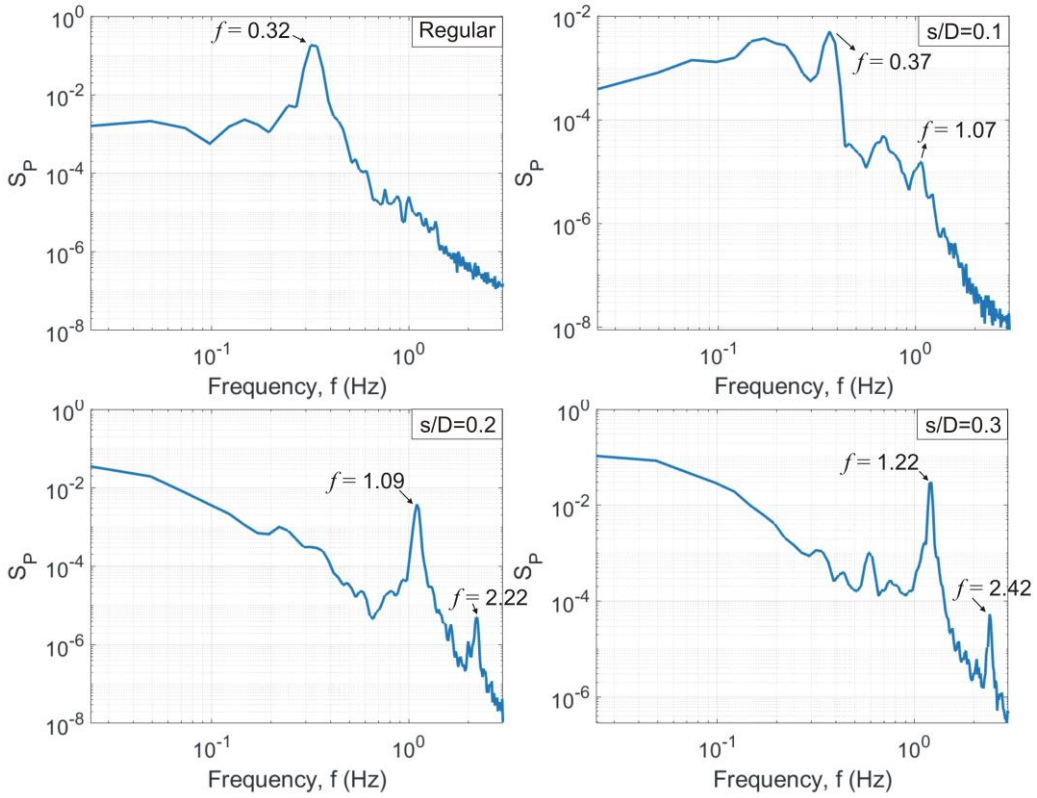

Figure 11. The spectral analysis of the lift coefficient, C_L, of the cylinders, S_p.

3.2. Velocity Field Results

In this section, both time-averaged and instantaneous velocity field results were presented and discussed. The results of time-averaged streamlines,$\langle\psi\rangle$, and velocity magnitudes, $(\langle u\rangle^2 + \langle v\rangle^2)^{1/2}/U_\infty$, of the flows around the regular and slit cylinders were presented in Figure 12. The flow structures, e.g., two focuses and one saddle point, in the downstream wake of the regular cylinder showed symmetry around the axis of the cylinder in the direction of the free-stream flow. On the other hand, in the cases of the slit cylinders, the slits, which connected the stagnation points on the front and the rear surfaces of the cylinders, generated a jet flow inside the downstream wake region. These jet flows emerging from the slit cylinders with s/D = 0.1 and 0.2 tried to divide the wake into two parts and increased the momentum of the flow inside the wake. Thus, the lengths of downstream wake regions of the slit cylinders with s/D = 0.1 and 0.2 became longer than that of the regular cylinder as presented in Figure 12, e.g., up to 33% longer length of the downstream wake was observed. In the case of the slit cylinder with s/D = 0.3, halves of the cylinder behaved like two separate bodies which were placed close to each other. Thus, separate wakes developed downstream of each half of the slit cylinder with s/D = 0.3. The length of the wake region downstream of the slit cylinder with s/D = 0.3 was significantly shortened when compared with the results of other slit cylinders with s/D $\leq$ 0.2 and the regular cylinder.

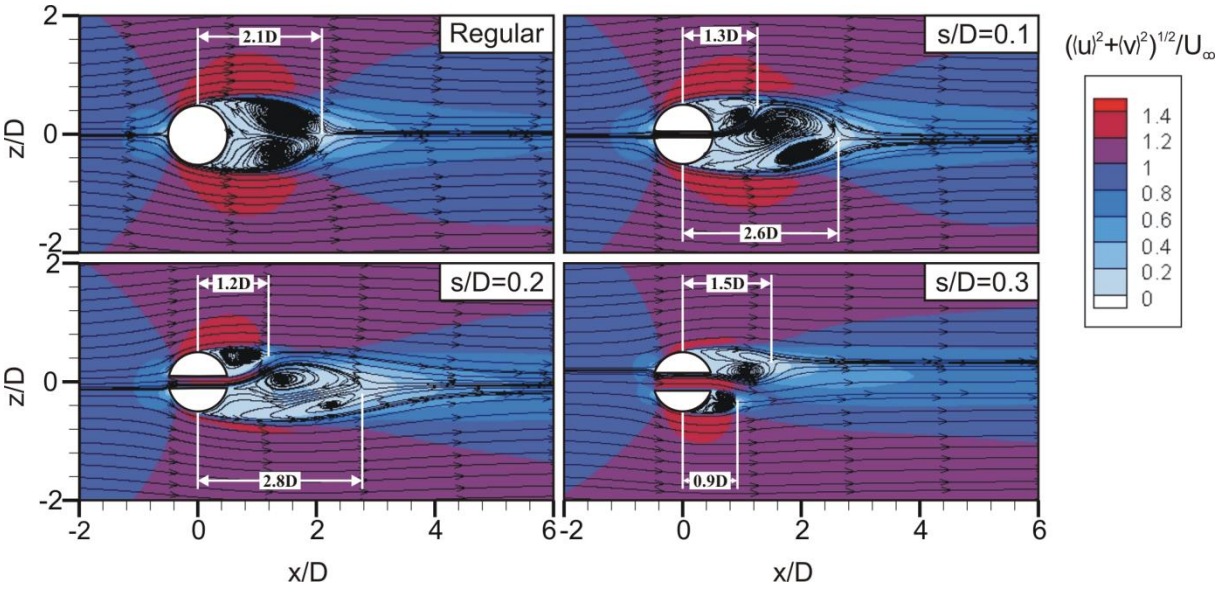

Figure 12. Patterns of mean streamlines, $\langle\psi\rangle$, and contours of mean velocity magnitude, $(\langle u\rangle^2 + \langle v\rangle^2)^{1/2}/\mathrm{U}_\infty$.

The jet flows emerging from the slits diverted in either right (or positive z-direction) or left (or negative z-direction) crossflow directions depending on the size of the s/D. Such as, whereas the jet flow diverted to the right crossflow direction (positive z-direction) for s/D = 0.1 and 0.2, it diverted to the left crossflow direction (negative z-direction) for s/D = 0.3. The directions of the jet flow's deviations were relevant to the locations of the separation points of the flow on the sides of the slit cylinders as presented in Table 2 previously. The locations of the stagnation points, θ_S, which formed on the front surfaces of the cylinders due to the incoming free-stream flow were also given in Table 2. Whereas one stagnation point developed on the front surface of the regular cylinder, two stagnation points developed on the front surfaces of each half of the slit cylinders because of the slits placed inside the cylinders. Similar to the asymmetry observed in the locations of the separation points, θ_{SP}, the locations of the stagnation points on the right and left parts of the front surfaces of the slit cylinders were asymmetric with each other. For example, whereas stagnation points formed at earlier locations on the right part of the slit cylinders with s/D = 0.1 and 0.2 than their left part with amounts of $\Delta\theta_{S,Front}$ = 0.5° and 1.5°, respectively, it formed earlier on the left part of the slit cylinder with s/D = 0.3 with an amount of $\Delta\theta_{S,Front}$ = 1.6°. As the slit width increased, amounts of the asymmetry between the locations of the stagnation points formed on the right and left surfaces of the slit cylinders increased. Thus, the change of the locations of the stagnation points and the separation points with a change in the slit width showed the same pattern which could be related to the deviation in the direction of the jet flow in the downstream wake region.

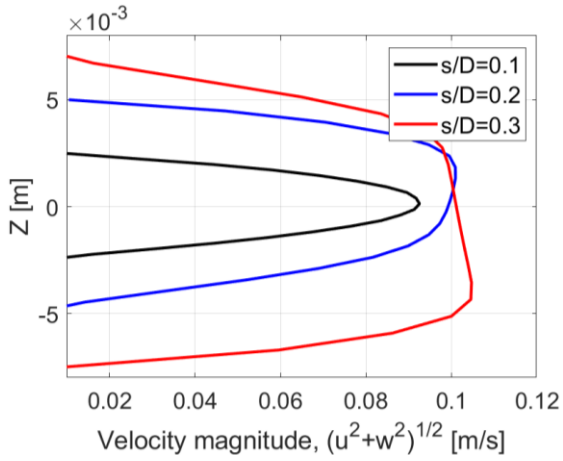

Figure 13. Profiles of the mean velocity magnitudes, $(\langle u\rangle^2 + \langle v\rangle^2)^{1/2}$, at the location of the slit exits for different slit width to cylinder diameter ratios, s/D.

Profiles of the time-averaged velocity magnitudes at the locations of the slit exits of each cylinder were given in Figure 13. Whereas the velocity magnitude results of the slit cylinder with s/D = 0.1 showed a symmetric profile, the results of the slit cylinders with s/D = 0.2 and 0.3 lost their symmetry and distorted in the same direction with the crossflow direction of the biased jet flow in the downstream wake. The momentum coefficients of each jet flow emerging from the slits with s/D = 0.1, 0.2, 0.3 were C_μ = 0.0092, 0.0265, 0.0474, respectively. Thus, as the slit width increased, the amount of momentum inserted by the jet flow inside the downstream wake increased. Accordingly, Gao et al. (2017b) had stated that the jet vortices became stronger with the increase of s/D value because the self-issuing jet was strengthened as the slit became larger. Ordia et al. (2017) had also stated that changing the slit width changed the flow resistance of the slit.

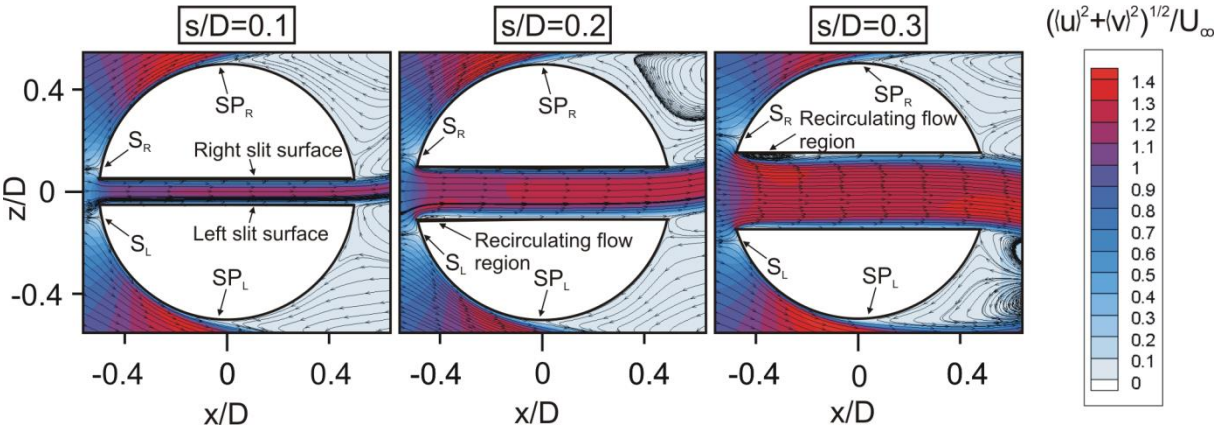

Figure 14. Close view of the contours of the velocity magnitude, $(\langle u\rangle^2 + \langle v\rangle^2)^{1/2}/U_\infty$, and time-averaged streamlines, $\langle\psi\rangle$, through the slits placed inside the cylinders.

In order to understand the effects of the slit's width on the jet flow, close views of the contours of the velocity magnitude and time-averaged streamlines through the slits of the cylinders were presented in Figure 14. Just after the entrance into the slits, recirculating flow regions formed on the inside surfaces

of the slit with s/D = 0.2 and 0.3. Whereas the recirculating flow region formed on the left surface inside the slit with s/D = 0.2, it formed on the right surface inside the slit with s/D = 0.3 with a larger size. These flow regions caused an asymmetric contraction in the cross-section of the jet flow at the entrance of the slits which distorted the velocity profiles of the jet flow through the end of the slits.

As presented in Figure 15(a), just after the inlet of the slits, sudden drops and then fast recoveries in the pressure coefficients occurred in short distances on the slit surfaces inside the cylinders. Accordingly, as presented in Figure 15(b), the friction coefficient results converged to zero after the entrance of the slits. Through the end of the slits, whereas a gradual decrease of the pressure coefficients occurred on the surfaces of the slits which are on the same side as the deviations of the jet flows, pressure recoveries occurred on the opposite surfaces of the slits. For example, there were pressure recoveries on the left surfaces of the slits with s/D = 0.1 and 0.2 and on the right surface of the slit with s/D = 0.3.

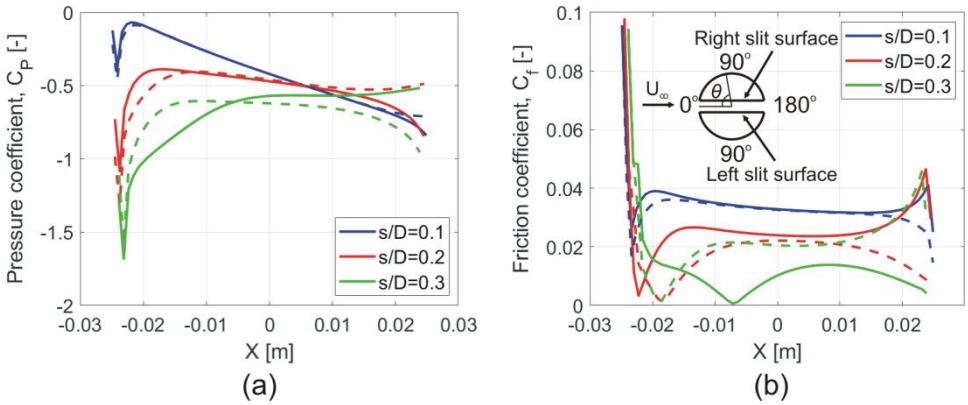

Figure 15. Pressure and friction coefficients on the slit surface inside the cylinders at y/D = 0. Solid and dashed lines show the results on the right and the left slit surfaces inside the cylinders, respectively.

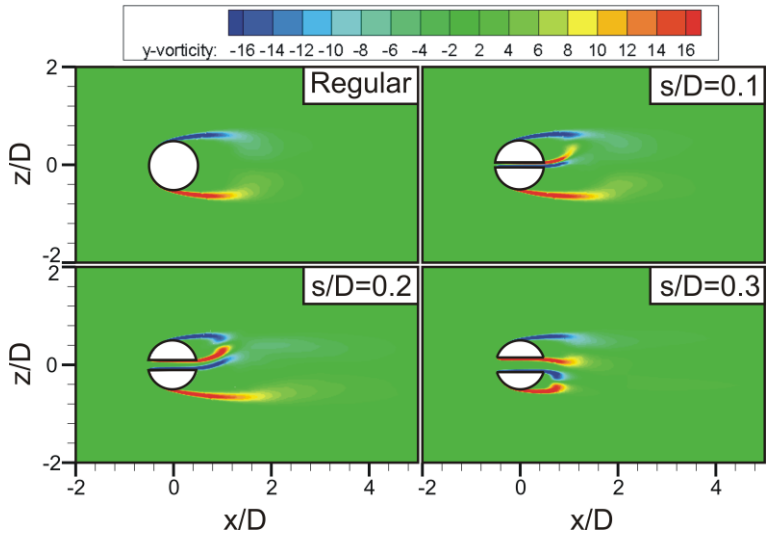

Figure 16. Mean vorticity, $\langle \omega_y \rangle$, concentrations in the vertical symmetry plane at y/D = 0. White and red dots on the figures represent the locations of the predominant shedding frequencies of the velocities.

Investigations of the characteristics of the vorticity concentrations around the cylinders can elaborate an understanding of the interaction between the jet flow due to the slits and the downstream wake. As presented in Figure 16, two symmetrically located vorticity concentrations which rotated in the opposite direction to each other formed on each side of the regular cylinder. On the other hand, the slit cylinders produced an additional vorticity concentrations pair which interacted with the outer vorticity concentrations due to the deviation of the jet flow in crossflow directions. As a result of these interactions between the inner and the outer vorticity concentrations, both the shape of the outer vorticity concentrations and their shedding characteristics were changed. For example, the length of the vorticity contours in the downstream wake of the slit cylinders with s/D = 0.1 and 0.2 increased when compared with that of the regular cylinder. Structures of the vorticity concentrations in the downstream wake of the slit cylinder with s/D = 0.3 looked like the structures of the vorticity concentrations which formed in the downstream wake of dual bluff bodies, e.g., side by side placed two cylinders (Afgan et al., 2011).

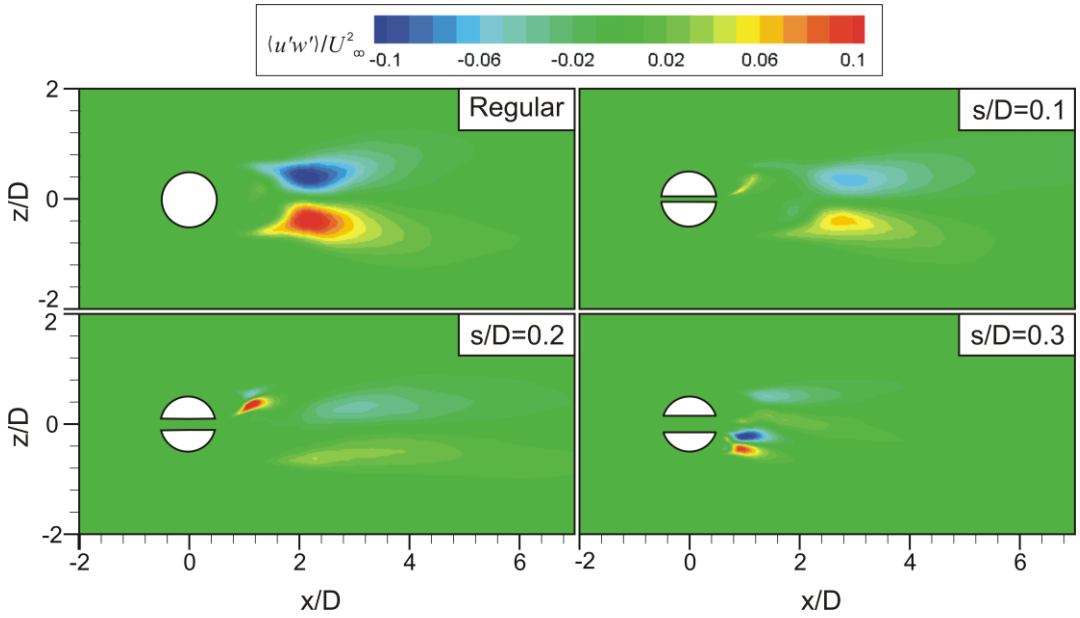

Figure 17. Contours of normalized mean Reynolds stress, $\langle u'w' \rangle / U^2_\infty$, in the vertical symmetry plane at y/D = 0. White and red dots on the figures represent the locations of the predominant shedding frequencies of the velocities.

Figure 17 revealed that the maximum magnitude of time-averaged Reynolds stress, $\langle u'w' \rangle$, in the downstream wake of the slit cylinder with s/D = 0.1 and 0.2 decreased dramatically when compared with the corresponding results of the regular cylinder due to the effects of the jet flow emerging from the slits. As a result of the jet flow, additional shear layers developed in the near wake of the cylinders which interact with the outer shear layers. Whereas the maximum value of the Reynolds stresses occurred in the far wake of the regular cylinder and slit cylinder with s/D = 0.1, their locations came closer to the near wake region of the slit cylinders with s/D = 0.2 and 0.3. In order to present the relationship between the Reynolds stresses and the shedding characteristics of the flow, the white and

red dots which show the locations of the predominant shedding frequency locations were left on the figures.

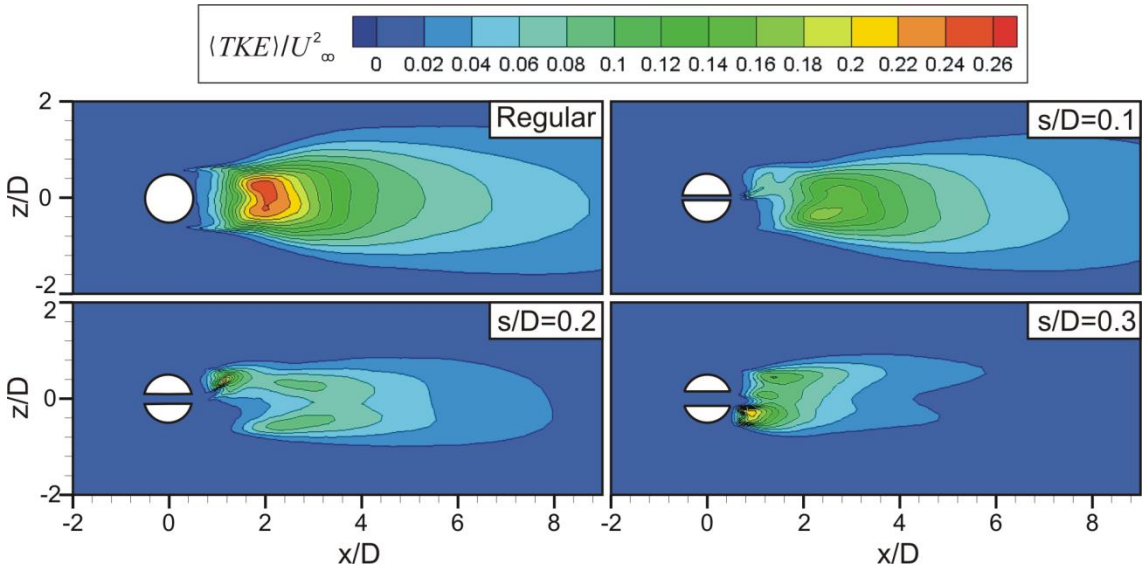

Figure 18. Contours of normalized mean turbulent kinetic energy, $\langle TKE \rangle / U_\infty^2$, in the vertical symmetry plane at y/D = 0.

Figure 18 apparently presented that the slits inserted inside the cylinder reduced both the maximum turbulent kinetic energy, TKE, and the size of its area covered in the downstream wake. On the other hand, in the near wake region of the slit cylinders with s/D = 0.2 and 0.3, new regions, in which the amount of the TKE increased, occurred.

4. Conclusion

The characteristics of flow around slit-inserted cylinders were investigated in the present study. In the investigations, three different slit width-to-diameter ratios, s/D = 0.1, 0.2 and 0.3, were used. The slits were placed inside the cylinders at a zero-inclination angle with incoming free stream flow.

The results presented that the slits inserted inside the cylinders modified the locations of critical flow points on their surfaces, e.g., locations of the stagnation and the separation points. For example, asymmetry happened between the locations of the stagnation and separation points on the right and left surfaces of the slit cylinders. Additionally, the slits caused the direction of the jet flows, which were occurred in the downstream wake of the cylinders, to deviate in the crossflow directions of the flow. As a result, the biased wake flow developed downstream of the slit cylinders. The characteristics of the downstream wake changed slightly in the case of the slit cylinder with s/D = 0.1 when compared to the regular cylinder. On the other hand, in the cases of slit cylinders with s/D = 0.2 and 0.3, both the shedding frequencies of the flow and the geometry of the wake flow downstream of the cylinders changed drastically. In all cases of the slit cylinders, while the drag coefficients of the slit cylinders decreased, their lift coefficients and Strouhal numbers increased. Finally, when compared

with the regular cylinder, the slit-inserted cylinders reduced the maximum value of TKE in their downstream wakes.

Acknowledgements

The author acknowledges the support of the Mechanical Engineering Department, Adana Alparslan Turkes Science and Technology University, for providing computational support for this study.

Disclosure statement

No potential conflict of interest was reported by the author.

Author's Contributions

The author's contributed to the study fully.

References

Afgan I., Kahil Y., Benhamadouche S., Sagaut P. Large eddy simulation of the flow around single and two side-by-side cylinders at subcritical Reynolds numbers. Physics of Fluids 2011; 23(075101):1-17. doi: 10.1063/1.3596267

Baek H., Karniadakis GE. Suppressing vortex-induced vibrations via passive means. Journal of Fluids and Structures 2009; 25:848 – 866. doi: 10.1016/j.jfluidstructs.2009.02.006

Bao Z., Qin G., He W., Wang Y. Numerical investigation of flow around a slotted circular cylinder at low Reynolds number. Journal of Wind Engineering and Industrial Aerodynamics 2018; 183:273–282. doi:10.1016/j.jweia.2018.11.010

Gao DL., Chen WL., Li H., Hu H. Flow around a slotted circular cylinder at various angles of attack. Experiments in Fluids 2017a; 58(132):1-15. doi:10.1007/s00348-017-2417-8

Gao DL., Chen WL., Li H., Hu H. Flow around a circular cylinder with slit. Experimental Thermal and Fluid Science 2017b; 82:287–301. doi:10.1016/j.expthermflusci.2016.11.025

Igarashi T. Flow characteristics around a circular cylinder with a slit (1st report, flow control and flow patterns). Bulletin of the JSME 1978; 21(154): 656-664.

Igarashi T. Flow characteristics around a circular cylinder with a slit (2nd report effect of boundary layer suction). Bulletin of the JSME 1982; 25(207):1389-1397.

Junwei W., Jinwen Y., Yi H., Feng B. Experimental study of slit cylinder vortex shedding in circulating water channel. International Conference on Measurement, Information and Control (MIC), 18-20 May 2012, 225-229, Harbin.

Kravchenko AG., Moin P. Numerical studies of flow over a circular cylinder at Re_D=3900. Physics of Fluids 2000; 12(2):403-417.

Olsen JF., Rajagopalan S. Vortex shedding behind modified circular cylinders. Journal of Wind Engineering and Industrial Aerodynamics 2000; 86:55-63.

Ordia L., Venugopal A., Agrawal A., Prabhu SV. Vortex shedding characteristics of a cylinder with a parallel slit placed in a circular pipe. Journal of Visualization 2017; 20:263–275. doi: 10.1007/s12650-016-0398-y.

Sheng WJ., Chen W. Features of flow past a circular cylinder with a slit. Sharif University of Technology Scientia Iranica Transactions B: Mechanical Engineering 2016; 23(5):2097-2112.

Williamson CHK. Vortex dynamics in the cylinder wake. Annual Review of Fluid Mechanics 1996; 28:477-539.